



Structured titanium oxynitride (TiO_xN_y) nanotube arrays for a continuous electrocatalytic phenol-degradation process: Synthesis, characterization, mechanisms and the chemical reaction micro-kinetics

Luka Suhadolnik^{a,*}, Damjan Lašič Jurković^{b,*}, Blaž Likozar^b, Marjan Bele^c, Sandra Drev^d, Miran Čeh^a

^a Department for Nanostructured Materials, Jožef Stefan Institute, Jamova 39, SI-1000, Ljubljana, Slovenia

^b Department of Catalysis and Chemical Reaction Engineering, National Institute of Chemistry, Hajdrihova 19, SI-1000, Ljubljana, Slovenia

^c Department of Materials Chemistry, National Institute of Chemistry, Hajdrihova 19, SI-1000, Ljubljana, Slovenia

^d Center for Electron Microscopy and Microanalysis, Jožef Stefan Institute, Jamova 39, SI-1000, Ljubljana, Slovenia

ARTICLE INFO

Keywords:

Electrocatalysis
Phenol degradation
TiON-nanotube catalyst
Electrically conductive nanotube arrays
Reaction mechanism

ABSTRACT

In this study a novel titanium oxynitride electrocatalyst was synthesized and its electrocatalytic activity for the degradation of phenol was evaluated. A highly conductive and efficient Ti–O–N electrocatalyst was prepared in a three-step synthesis. A titanium coil was anodized to grow TiO_2 nanotubes, which were then annealed in air to convert the amorphous structure to anatase and afterwards annealed in ammonia to obtain the final Ti–O–N catalyst. This was characterized with X-ray diffraction (XRD), X-ray photoelectron spectroscopy (XPS), scanning electron microscopy (SEM), transmission electron microscopy (TEM) and selected-area electron diffraction (SAED). To evaluate its degradation capabilities, the electrocatalytic oxidation of the phenol was performed inside a coil-type electrocatalytic microreactor. Phenol conversions of up to 95% of the initial 0.4 mmol L^{-1} of phenol were achieved at the studied applied electric potentials (1–16 V), NaCl concentrations ($0.51\text{--}5.12 \text{ g L}^{-1}$) and flow rates ($20\text{--}500 \mu\text{L min}^{-1}$). The mechanism of electrocatalytic oxidation was proposed in a three-dimensional reactor model that accurately describes the electrocatalytic degradation of phenol at the Ti–O–N anode in the presence of NaCl in the phenol solution. It was shown that both OH^{\bullet} – and OCl^{\bullet} –mediated reaction mechanisms contribute to the phenol's degradation, while at high NaCl concentrations (5 g L^{-1}) the latter is dominant. In addition, the optimal reactor design is determined by studying the mass-transfer limitation with the model.

1. Introduction

The electrocatalytic degradation of organics is one of the most promising methods for the elimination of toxic organic compounds from polluted water with medium flow rates. It is an advanced, green oxidation process, since the required electrical energy can be provided by renewable sources [1,2]. The electrocatalytic reaction takes place on the surface of an electrocatalyst or in the bulk of the solution, depending on the type of active species involved in the degradation reactions. The most important active species are the hydroxyl species and active chlorine (in the case that a chlorine source is present in the electrolyte), which are all generated electrochemically on the catalyst's surface [3,4]. An ideal electrocatalyst exhibits a very high surface area, long-term stability, high current efficiency and is at the same time inexpensive to produce.

There have been many reports on the electrocatalytic degradation of organic contaminants using a variety of different electrode materials, among which boron-doped diamond (BDD) [5–7], dimensionally stable electrodes (DSA) [8,9], platinum [10], metal oxides (e.g., PbO_2 , SnO_2) [11,12], graphite [13], and activated carbon fiber [14] were given the most attention. These studies showed that BDD electrodes are the most efficient for phenol removal due to their high oxygen overpotential. However, these electrodes are not the most suitable for industrial use, due to their high cost and energy consumption. Moreover, there is a strong possibility of BDD film delamination [15]. Therefore, an efficient, cost-effective and stable electrocatalyst that has the potential for applications in wastewater treatment has still to be found.

In the search for an efficient, alternative electrocatalyst, titanium oxynitride has been identified as a very promising candidate. According to the chemical composition, it is similar to titanium dioxide (TiO_2),

* Corresponding authors.

E-mail addresses: luka.suhadolnik@ijs.si (L. Suhadolnik), damjan.lasic@ki.si (D. Lašič Jurković).

<https://doi.org/10.1016/j.apcatb.2019.117894>

Received 25 March 2019; Received in revised form 11 June 2019; Accepted 19 June 2019

Available online 21 June 2019

0926-3373/ © 2019 Elsevier B.V. All rights reserved.

which is used for photocatalytic decomposition, but is not sufficiently electrically conductive to be suitable for electrocatalytic decomposition, which in some instances is preferable, because of its greater efficiency. Titanium oxynitride exhibits interesting physical, electronic, optical and catalytic properties that can be tuned with the oxide/nitride ratio [16,17]. Moreover, it already demonstrated its ability to drive various electrocatalytic reactions. It was employed in different fields of research and showed great potential in numerous applications, including water splitting [18] (either as an electrode for a hydrogen-evolution reaction or an oxygen-evolution reaction), fuel cells [19], lithium-ion batteries [20], photocatalytic degradation [21], thermal solar collectors [22] and electrically switchable windows [23]. However, titanium oxynitride has, to the best of our knowledge, never been used for the electrocatalytic degradation of organic compounds.

One type of common organic pollutant that has been extensively studied is the aromatic compounds, which are present in the wastewater of many chemical plants. Among them, phenol was mostly used as a model organic compound for electrocatalytic degradation studies among which anodic oxidation and electro-Fenton processes were given the most attention [24,25]. It was found that phenol is usually first oxidized to aromatic intermediates (benzoquinone, hydroquinone and catechol) followed by the formation of aliphatic acids (maleic, oxalic, fumaric) [26] or total mineralization [27]. The type of intermediate products formed and the extent of the degradation mostly depends on the choice of the electrode materials and the presence of inorganic ions in the electrolyte. However, chloride ions in the electrolyte cause the largest increase in the degradation efficiency due to the generation of an active chlorine species (chlorine, hypochlorite acid and hypochlorite).

The first study of electrochemical phenol oxidation in the presence of sodium chloride took into account only the direct oxidation of the phenol [28], while the mechanism for the oxidation of the pollutants in the presence of NaCl was proposed later by Comninellis and Nerini [9]. It describes the direct and indirect oxidation of phenol and the reactions occurring at the anode and the cathode during electrocatalytic oxidation. However, the paper does not describe these processes with a mathematical model that can provide useful information about the kinetics of the electrocatalytic reactions, the adsorption properties of the catalyst and can be used to determine the most efficient design of the electrocatalytic system [29]. Mathematical models can be used for both predicting and understanding the electrocatalytic processes and have to be developed, step-by-step, towards a full description of the governing processes occurring inside the electrocatalytic systems.

In the present work we report on a new type of electrocatalyst for the electrocatalytic degradation of organics. The developed Ti–O–N electrocatalyst was synthesized with an anodic oxidation process, followed by annealing in an air and ammonia atmosphere. The method enables the rapid and low-cost synthesis of rigidly attached Ti–O–N nanotubes on the titanium substrate. The catalyst was characterized in terms of its structure and chemical composition (XRD, XPS, SEM and TEM) and its efficiency and stability for the phenol-degradation reaction (SEM and HPLC). The electrocatalytic degradation of phenol was carried out inside a continuous-flow coil-type microreactor in the presence of the NaCl electrolyte. The electrocatalytic degradation was described using a three-dimensional mathematical model, which includes the contribution of the oxidation with Cl^- -based reaction pathways.

2. Experimental

2.1. Synthesis of Ti–O–N nanotubes

The Ti–O–N nanotube film was prepared using an anodic oxidation process followed by two annealing procedures in different atmospheres. In the first step, the TiO_2 nanotube arrays were grown by the anodic oxidation of a titanium coil made of titanium wire (250 μm diameter,

99.8%, Advent Research Materials Ltd.). The titanium coil was first cleaned with acetone and ethanol in an ultrasonic bath. After the cleaning, the coil was anodized in a viscous organic electrolyte consisting of ethylene glycol (99.5%, Merck) with the addition of 0.3 wt.% ammonium fluoride (99.99%, Sigma-Aldrich) and 2 vol.% deionized water. A constant electrical potential of 60 V was applied to the electrodes using a DC power supply (Toellner) and the titanium coil was anodized for 6 h. The as-anodized titanium coil was washed with deionized water and ethanol and calcined at 450 °C for 1 h in air (the heating and cooling rate was 5 °C min^{-1}). The second annealing was performed in an ammonia atmosphere at 700 °C for 10 h to produce the desired Ti–O–N nanotube arrays. The flow of ammonia gas was kept constant at 50 $\text{cm}^3 \text{min}^{-1}$.

2.2. Characterization of the materials

The morphological characterization of the Ti–O–N arrays was made in a field-emission scanning electron microscope (FSEM) (Jeol JSM-7600F) and in a transmission electron microscope (TEM) (Jeol JEM-2100, Jeol JEM-2010F). Prior to the FSEM observations the samples were coated with a thin layer of carbon to ensure the electrical conductivity of the samples. For the TEM observations the Ti–O–N nanotubes were separated from the metal Ti and sputtered onto the lacy carbon TEM grids. The Ti–O–N film was also characterized with X-ray diffraction using a D5000 Bruker AXS diffractometer with $\text{Cu-K}\alpha$ radiation ($\lambda = 1.5406 \text{ \AA}$). The diffractograms were measured in the 2θ angular range between 30 and 100° with a step size of 0.04° and a collection time of 1 s. The phase identification was performed with the X'Pert HighScore Plus program using the International Centre for Diffraction Data (ICDD) PDF-4 + 2016 database [30]. The surface of the Ti–O–N film (upper 3–5 nm) was also characterized using X-ray photoelectron spectroscopy (XPS) on a PHI-TFA XPS spectrometer produced by Physical Electronics Inc. The samples were introduced into the ultra-high vacuum (10^{-9} mbar during analysis) spectrometer and the high-energy-resolution spectra were acquired at constant pass energy of 29 eV. The energy analyzer was operating at a resolution of 0.6 eV. The quantification of the surface composition was carried out using Multipak software, version 8.0 from Physical Electronics Inc. The spectra were aligned by setting the C 1s peak to 284.8 eV, characteristic for C–C/C–H bonds. The binding energies shift was about ± 0.3 eV. The background was removed using the Shirley function and the high-resolution spectra were fitted with Gauss-Lorentz functions.

2.3. Fabrication and assembly of a coil-type electrocatalytic microreactor

The coil-type electrocatalytic microreactor was fabricated according to the procedure reported by Suhadolnik et al. [31]. In brief, the Ti–O–N coil with a length of approximately 64 mm was placed in the middle of a 3-mm-diameter silica glass rod with a length of approximately 102 mm. On each side of the anodized anode coil, a cathode coil with a length of approximately 12 mm was placed. The cathode coils were made of 250- μm titanium wire. The electrodes were separated by 2-mm plastic spacers to prevent a short circuit. The active unit of the electrocatalytic reactor was placed inside a Plexiglas (Acrytech d.o.o.) housing with a mechanically engraved cylindrical channel. The calculated surface of the Ti–O–N coil was approximately 9.5 cm^2 , if only the geometric area of the nanotube film is taken into account. The calculated surface area of each titanium cathode was approximately 1.78 cm^2 . The distance between the outer diameter of the coils and the inner radius of the channel in the housing was approximately 200 μm . The microreactor volume in the part of the electrodes was approximately $166 \pm 10 \mu\text{l}$.

2.4. Electrocatalytic degradation of phenol

The electrocatalytic efficiency of the Ti–O–N nanotube arrays was

investigated by measuring the degradation of phenol inside the coil-type electrocatalytic reactor. The initial phenol (99.9%, Sigma-Aldrich) solution with a concentration of approximately 50 mg L^{-1} was introduced into the reactor through the inlet channel. Fluorinated ethylene propylene tubing (internal diameter of 0.5 mm, Vici AG International) was used to connect the inlet of the reactor with a syringe pump (Harvard Apparatus). The volumetric flow rate of the phenol solution was in the range $20\text{--}500 \text{ }\mu\text{L min}^{-1}$. The reactor volume being $166 \text{ }\mu\text{L}$, these flow rates correspond to the residence times (reactor volume divided by the flow rate) between 8.3 min and 0.332 min. The phenol solution was prepared by dissolving it in deionized water. The electrolyte conductivity was varied from 1 mS cm^{-1} to 10 mS cm^{-1} with the addition of sodium chloride (99.99%, Acros Organics) and measured with a ProLine Plus M330 conductivity meter. The applied electric potential to the electrodes in the reactor was in the range $0.2\text{--}16 \text{ V}$. The phenol solution (1.5 mL) was pumped through the reactor before each measurement in order to clean the reactor and reach a steady state. Afterwards, the samples were collected at the outlet of the reactor and analyzed with a high-performance, liquid chromatograph (HPLC, Agilent 1100 Series). The adopted HPLC method [32] enabled us to detect the phenol and its degradation products. The amount of degraded phenol and the amounts of intermediates produced were determined from the calibration curves. The HPLC was equipped with a solvent-delivery pump (G1312A) with a Phenomenex (Torrance, CA) SynergiTM 4- μ Hydro-RP 80 \AA analytical column ($250 \times 4.6 \text{ mm}^2$, 4- μm packing) and a UV-vis detector (G1315A). The solvent was a 70:30 (vol:vol) mixture of Milli-Q water and acetonitrile. The phenol and its degradation products were analyzed at 254 nm. The retention times for the phenol and benzoquinone were 9.3 and 5.7 min. The error in determining the concentration was estimated to be $\pm 5\%$ in the case of phenol and $\pm 10\%$ in the case of benzoquinone. In addition to the phenol and benzoquinone, which was the only intermediate we observed, calibration curves were also made for hydroquinone, catechol and pyrogallol. However, there were no additional identified and unidentified peaks visible other than that of phenol and benzoquinone when analyzing our samples.

Total organic carbon (TOC) content of the liquid product stream was determined with Rosemount Analytical Dohrmann DC-190 TOC analyser. It corresponded to the amount of residual organic byproducts of phenol mineralization as well as the unconverted phenol.

The same procedure was used to determine the electrocatalytic activity of TiO_2 nanotubes, which was done in order to compare the activities of Ti-O-N and TiO_2 . The latter catalyst was annealed only at 450°C and used inside the coil-type reactor.

3. Modeling

3.1. Mechanism of electrocatalytic phenol oxidation

The proposed model mechanism for phenol oxidation on the Ti-O-N surface is presented in Fig. 1. It is adopted from what is commonly observed in the literature [4]. It is important to distinguish between surface and bulk reaction mechanisms. The mechanisms can change entirely depending on the reaction phase under different conditions. This is seen for example in the literature for the case of electrochemical reduction of furfural, where the usage of copper electrodes, pure or modified with different types of organothiols, resulted in different ratios of electro catalytic and electrochemical mechanisms, greatly affecting the product distribution and yields [33]. In the literature, multiple sources state that the dominant reaction takes place on the catalytic surface, both for Cl mediated [34,35] and OH mediated mechanisms [36–38,31]. As noted in [38], the adsorption of organics to the electrode results in longer lifetimes of the species at the electrode surface, which enables a higher probability of oxygen transfer, as well as a higher degree of the aromatic molecule destabilization when it is strongly adsorbed.

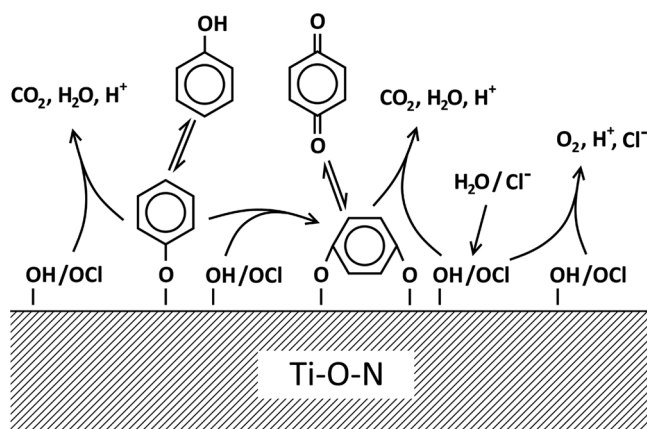


Fig. 1. Proposed and modelled mechanism for phenol electrocatalytic oxidation on the Ti-O-N surface.

After the phenol is adsorbed to the surface, it can undergo partial oxidation to benzoquinone or total oxidation to CO_2 . The latter generally proceeds through different shorter-chain intermediates such as carboxylic acids – since these reactions are usually fast, we excluded them from our model and assumed the instantaneous oxidation of these intermediates to the final products. Benzoquinone can itself be either further oxidized to CO_2 , or desorbed from the surface as a side product. From our experimental data, it was evident from the concentration profiles that benzoquinone is a side product rather than the main oxidation intermediate.

All of the reactions of the proposed mechanism are presented in Table 1. We based the reaction network on our previously published modelling efforts [31], as well as the general observations seen in the available literature, as is discussed below. The actual electrochemically dependent reaction network part is the generation of the active species (reactions #4 and #8). The rates of these reactions depend on the applied voltage. Electrons are excluded from the reactions for simplicity. * represents a binding site on the surface of the catalyst. Based on the available literature [4,37], we have decided to treat the OH^* species as the main water-based reactive oxidant, which is formed via direct water splitting (reaction #4). In addition, oxygen can be transferred through Cl^- -based reaction pathways, usually through the OCl^* surface intermediate [4,39,35,37,40,41,34], formed through the dissolved chloride ions (reaction #8). Both OH^* and OCl^* species can also be consumed through various reactions, like recombination [42–44] – generally, most of these reactions follow second-order kinetics, and we have coupled them all under reactions #12–14. Note that these active species could combine either to form water, Cl^- , O_2 or H^+ . Since none of these species affects the overall model kinetics, there is no effect on the exact pathway of their recombination. All of the bulk species can be adsorbed to and desorbed from the active catalyst surface (reactions #1–3) [38], and it was assumed that the water would always be in steady-state surface coverage due to it being in excess. It was also assumed that the oxygen, once generated, desorbed immediately. The concentration of protons was not modelled, as it is expected that they are transferred to the cathode, where H_2 is formed. Reactions #5–7 and #9–11 represent the oxidation reactions of phenol and benzoquinone through the OH^* and OCl^* species, respectively [38]. For reactions #5, #7, #9 and #11, the reaction rate was first-order dependent on the OH^* and OCl^* concentrations. This is due to the reaction being a conglomerate of multiple, underlying first-order reaction pathways through short-lived oxidation intermediates. The reaction rate constants, shown in Table 1, were obtained by means of numerical parameter regression using the model and our experimental data, as described in more detail in the model development section below.

Table 1
Surface reaction network and the fitted parameter values.

#	Reagents		Products	k_{forward}	k_{backward}
1	$\text{C}_6\text{H}_5\text{OH} + *$	\rightleftharpoons	$\text{C}_6\text{H}_5\text{OH}^*$	$1.14\text{E} + 06 \text{ L mol}^{-1} \text{ s}^{-1}$	$3.16\text{E} + 04 \text{ s}^{-1}$
2	$\text{C}_6\text{H}_4\text{O}_2 + *$	\rightleftharpoons	$\text{C}_6\text{H}_4\text{O}_2^*$	$2.27\text{E} - 15 \text{ L mol}^{-1} \text{ s}^{-1}$	$1.55\text{E} + 00 \text{ s}^{-1}$
3	$\text{CO}_2 + *$	\rightleftharpoons	CO_2^*	$8.85\text{E} - 14 \text{ L mol}^{-1} \text{ s}^{-1}$	$7.77\text{E} + 02 \text{ s}^{-1}$
4	$\text{H}_2\text{O} + *$	\rightarrow	$\text{OH}^* + \text{H}^+$	$7.17\text{E} + 00 \text{ L mol}^{-1} \text{ s}^{-1}$	/
5	$\text{C}_6\text{H}_5\text{OH}^* + 11 \text{ OH}^*$	\rightarrow	$6 \text{ CO}_2^* + 6 * + 17 \text{ H}^+$	$2.03\text{E} + 02 \text{ s}^{-1}$	/
6	$\text{C}_6\text{H}_5\text{OH}^* + \text{OH}^*$	\rightarrow	$\text{C}_6\text{H}_4\text{O}_2^* + * + 3 \text{ H}^+$	$7.78\text{E} + 07 \text{ s}^{-1}$	/
7	$\text{C}_6\text{H}_4\text{O}_2^* + 10 \text{ OH}^*$	\rightarrow	$6 \text{ CO}_2^* + 5 * + 14 \text{ H}^+$	$1.63\text{E} - 08 \text{ s}^{-1}$	/
8	$\text{Cl}^- + \text{H}_2\text{O} + *$	\rightarrow	$\text{OCl}^* + 2 \text{ H}^+$	$1.35\text{E} + 04 \text{ L mol}^{-1} \text{ s}^{-1}$	/
9	$\text{C}_6\text{H}_5\text{OH}^* + 11 \text{ OCl}^*$	\rightarrow	$6 \text{ CO}_2^* + 6 * + 11 \text{ Cl}^- + 6 \text{ H}^+$	$1.25\text{E} + 09 \text{ s}^{-1}$	/
10	$\text{C}_6\text{H}_5\text{OH}^* + \text{OCl}^*$	\rightarrow	$\text{C}_6\text{H}_4\text{O}_2^* + * + \text{Cl}^- + 2 \text{ H}^+$	$5.51\text{E} + 05 \text{ s}^{-1}$	/
11	$\text{C}_6\text{H}_4\text{O}_2^* + 10 \text{ OCl}^*$	\rightarrow	$6 \text{ CO}_2^* + 5 * + 10 \text{ Cl}^- + 4 \text{ H}^+$	$1.12\text{E} - 10 \text{ s}^{-1}$	/
12	2 OCl^*	\rightarrow	$2 * + \text{O}_2 + 2 \text{ Cl}^-$	$2.53\text{E} + 12 \text{ s}^{-1}$	/
13	$\text{OH}^* + \text{OCl}^*$	\rightarrow	$2 * + \text{Cl}^- + \text{O}_2 + \text{H}^+$	$3.38\text{E} + 13 \text{ s}^{-1}$	/
14	2 OH^*	\rightarrow	$\text{O}_2 + 2 * + 2 \text{ H}^+$	$1.52\text{E} + 14 \text{ s}^{-1}$	/

3.1.1. Effects of the applied voltage and NaCl concentration

As widely shown in literature [4] and also observed in our previous study [31], the use of a NaCl solution electrolyte seems to induce a higher degradation of organic pollutants due to the Cl^- -mediated oxygen-transfer reactions. As no chlorinated products were detected, we assumed a simplified mechanism where the Cl^- ions can transfer oxygen in a similar fashion to the OH^* species, but through the OCl^* intermediate, as was also observed and discussed in the literature [39,35,37,40,41,34]. In the model, the effect of voltage on the reaction rates was only through the rate of generation of the OH^* and OCl^* active species, both through water splitting and Cl^- -transfer reactions. The constants of the respective reactions (#4 and #8) therefore depend on the applied voltage, as seen in Eq. (1). k_{max} in this case is equal to the kinetic constant value from Table 1, U denotes voltage, and $k(U)$ denotes the value of the reaction constant at a certain applied voltage.

$$U > 1.2 \text{ V}, k(U) = k_{\text{max}} \frac{U}{16 \text{ V}} / U \leq 1.2 \text{ V}, k(U) = 0 \quad (1)$$

The effect of voltage on the reaction constant is linear, with the exception of the initial cut-off voltage, which we have determined to be 1.2 V, based on the regression of all of our combined experimental efforts, as discussed in the results section. In addition, the generation of the OCl^* species (reaction #8) also depends on the Cl^- concentration, which we assumed was constant, due to it being in excess and only depended on the dissolved NaCl concentration. In our model we have assumed that the active surface species (OH^* and OCl^*) can recombine in various ways, resulting in a second-order reaction of their consumption. This leads, mechanistically, to diminishing returns when increasing the voltage, as the surface coverage of the active oxidants reaches a plateau.

3.2. Reactor and kinetics model development

3.2.1. Surface mass balances

The full kinetic network described above was simplified by removing the irrelevant reaction rates. For example, water could be completely removed as a species in the system, due to it being in large excess. Likewise, it is assumed that oxygen is desorbed very quickly and contributes minimally to the reaction. For the above reactions, the reaction rates are calculated for each reaction using Eq. (2), and then the surface-species coverage balances are calculated using Eq. (3).

$$r_n = k_{\text{for}} \theta_{r,1}^{N_{r,1}} \theta_{r,2}^{N_{r,2}} \dots - k_{\text{back}} \theta_{p,1}^{N_{p,1}} \theta_{p,2}^{N_{p,2}} \dots \quad (2)$$

R_n is the n -th reaction, k_{for} and k_{back} are the forward and reverse reaction rates, $\theta_{r,x}$ and $\theta_{p,x}$ are the coverages of each reagent and product in the reaction (which are replaced by the concentration if the reagent is a bulk species), and $N_{r,x}$ and $N_{p,x}$ indicate the reaction order of the species.

$$\frac{d\theta_i}{dt} = \sum_{n=0}^{N_{\text{reac}}} r_n S_{n,i} \quad (3)$$

N_{reac} is the total number of reactions, and $S_{n,i}$ is the stoichiometric factor of the species for the reaction. The coverage derivatives are used to calculate the transient changes in the surface coverages of the adsorbed intermediates, and the fictional bulk surface-coverage changes are used to link the surface reactions to the bulk changes in the concentration, as described below.

3.2.2. Bulk-species mass balances

A three-dimensional reactor model was developed to simulate the experimental system. The model included mass transport in the form of lateral convection and lateral as well as radial diffusion. The reaction took place on the inner electrode only, and the reagents reached the surface via radial diffusion.

For every point in the reactor, the following equation (Eq. (4)) can be used to describe the temporal derivative of the concentration of the bulk species.

$$\frac{\partial C_i}{\partial t} = -v_x \frac{\partial C_i}{\partial x} + D_i \frac{\partial^2 C_i}{\partial x^2} + D_i \frac{1}{r} \frac{\partial^2 C_i}{\partial r^2} + \frac{d\theta_i}{dt} C^* \quad (4)$$

v_x is the velocity in the lateral direction at a certain r , D_i is the diffusion coefficient of the bulk species, and C^* is the concentration of active sites in the discretized volume. After the equation's discretization (10 points along the reactor length and 10 points along the radial direction), a set of numerically solvable, ordinary differential equations was obtained.

The diffusion constant of phenol was taken to be $10^{-9} \text{ m}^2 \text{ s}^{-1}$, as found in the literature [45]. The diffusion constant for benzoquinone was assumed to be equal to that of phenol, due to the very similar structure and molecule size. The velocity distribution was assumed to be parabolic with regards to the radial dimension (Eq. (5)), as is the case for a laminar flow between two parallel plates, and was a good approximation in our case.

$$v_x = v_{x,\text{max}} \left(1 - \left(\frac{(r - R_{\text{inner}}) - (R_{\text{outer}} - R_{\text{inner}})/2}{(R_{\text{outer}} - R_{\text{inner}})/2} \right)^2 \right) \quad (5)$$

$v_{x,\text{max}}$ is the maximum velocity and R_{inner} and R_{outer} are the radii of the inner electrode and the outer wall, respectively. The reactor volume was 166 μL , the length of the reactor was 64 mm, the distance between the walls of the reactor was 0.2 mm and the inner diameter was 3.5 mm. An estimated 10^{-7} moles of surface sites per liter of reactor volume was determined by the model to be the available surface-site concentration, with adsorbed water covering the rest.

The boundary conditions were as follows. For the differential volumes at the reactor outer wall, no diffusion was permitted in the wall direction. Likewise, for the volumes at the reactor outlet, no diffusion was permitted to the after-reactor volume, as we assumed that the

concentration in that region is the same as in the last reactor point. Danckwerts boundary conditions were assumed at the reactor inlet, but the change in the concentration just before the reactor due to diffusion was not modeled, rather it was assumed to always be in the steady state. At the differential volumes by the reactive surface, the surface reaction proceeded. Model validation was carried out by checking the mesh independence at the discretization levels used, as well as checking the results with different input absolute and relative tolerances to the solver.

3.2.3. Solving the equations and kinetic parameters numerical regression

Numerical time-integration and regression were performed with a combination of Python and C. A backwards-differentiation formula, variable-order-based solver (CVODE solver [46] from the Sundials library [47]) was used for solving the system of ordinary differential equations. The verification of the model was confirmed by checking for spatial mesh-independence. This was done by varying the amount of discretization volumes and checking the convergence of the solution to the same result. Additionally, the temporal discretization and numerical stability errors were checked by varying the solver's absolute and relative tolerances. In all cases, the system was modelled for enough model time to reach steady state.

The reaction rate constants (as shown in Table 1) were obtained by fitting the model parameters to the experimental data using the COBYLA [48] numerical regression scheme, implemented in the SciPy [49] Python library. The process is a derivative-free algorithm for constrained optimization which utilizes linear approximation. The sum of squared differences between experimental and model reactor outlet phenol and benzoquinone concentrations was used as the objective value, which was minimized by the regression algorithm. The procedure was repeated multiple times using different initial values for the kinetic parameters, both randomly generated and directly estimated, to ensure the parameter values converged to the same global minimum, and for covering a larger parameter space.

4. Results and discussion

4.1. Characterization of the Ti–O–N nanostructures

The surface morphology of both the unused and used Ti–O–N nanotube arrays on the Ti wire substrate were observed and directly compared using the FSEM at the same magnifications (Fig. 2). The micrographs of the unused anodized coils are denoted a, b, and c, while the surfaces of the used anodized coils are denoted a*, b* and c*. The low-magnification micrographs (Fig. 2a, a*) show that both anodized surfaces are cracked, which is due to the annealing treatment where the crystallization occurs as well as due to the relatively small curvature radius of the metallic Ti wire. The comparison of both nanotubes' surface morphologies taken at $3000\times$ magnification (Fig. 2b, b*) shows that the nanotubes that were used in the degradation experiments are somewhat joined together, most likely due to the flow of the liquid medium and due to the applied electric potential. We believe that the first time high voltages are applied, there might be some immediate change in surface morphology, which then remains the same throughout the experiments. This is due to some expected minor rearrangements of the surface in the applied electrovoltaic field. Higher-magnification micrographs (Fig. 2c, c*) reveal that individual nanotubes are polycrystalline in nature with the sizes of the individual grains up to 50 nm. In addition, a similar catalyst activity was observed over the timeframe of the activity measurements (Fig. S4). The difference between the values correspond to both, the change in morphology and the experimental error.

The phase composition of the electrocatalyst was determined with X-ray powder diffraction (XRD). The XRD spectra in Fig. 3 show a titanium oxynitride coating on titanium. The peaks (circles) correspond to titanium oxynitride, peaks (T) to titanium and peaks (x) to titanium

nitride. The major diffraction peaks in the XRD spectra correspond to the cubic titanium oxynitride at 37° (111), 43° (200) and 63° (220) 2θ angles (PDF 01-084-4872) [30], the hexagonal titanium substrate at 38° (002), 40° (101), 53° (102), 70° (103) 81° (004) and 92° (104) 2θ angles (PDF00-001-1197) [30], and the tetragonal titanium nitride at 39° (111) and 41° (210) 2θ angles (04-001-9127) [30]. There is no diffraction peak of TiO_2 anatase phase, meaning it was converted entirely into titanium oxynitride during annealing in the ammonia atmosphere. The XRD analysis shows that the formation of the titanium oxynitride occurred throughout the entire depth of the sample, although the exact stoichiometry of the titanium oxynitride was only determined on its surface. However, the electrocatalytic reactions take place on the surface of the catalyst, rendering the information about the surface composition the most important for the purpose of this study.

The surface concentrations of the titanium, oxygen and nitrogen elements were determined with X-ray photoelectron spectroscopy (XPS). Quantification of the surface composition was performed using the XPS peak intensities, taking into account the relative sensitivity factors. We estimate that the relative error of the calculated concentrations is about 20% of the reported values. XPS spectra of the titanium oxynitride electrocatalyst (Fig. 4a) show the Ti–O–N compound with a composition around 1:1:1. The N 1s spectrum (Fig. 4b) is a very characteristic spectrum for nitride N^{3-} in the TiN compound. The peak at 397.0 eV corresponds to the nitride, while the peak at 299.2 eV is ascribed to the oxynitride. Approximately half of the titanium is present in the Ti^{4+} oxidation state (Fig. 4c). The rest of the titanium is in the Ti^{3+} (app. 25%) and Ti^{2+} (25%) oxidation states due to the Ti–nitride bonds.

An additional microstructural characterization of the Ti–O–N nanostructures was performed in the TEM. Fig. 5 shows a typical bright-field TEM micrograph of a Ti–O–N nanotubes sample that is composed of nanosized Ti–O–N grains. A partially broken nanotube, marked with arrows, can also be observed. The Ti–O–N nanotubes are polycrystalline in nature with an average grain size of a few tens of nanometers. The selected-area electron-diffraction pattern (SAED) acquired from the region shown in Fig. 5 clearly confirms the data obtained by the XRD. Namely, all the diffraction peaks can be assigned to the cubic oxynitride based on a comparison of the experimental and calculated diffraction peaks in the SAED pattern.

A side-view of the Ti–O–N nanotubes can be seen in Fig. 6a, while the inner and outer diameters of the nanotubes were estimated from the cross-section projection of the nanotubes (Fig. 6b) to be 50–70 nm and 120–150 nm, respectively.

4.2. Phenol degradation

The fitted kinetic parameters for the electrocatalytic degradation of the phenol obtained by numerical regression are presented in Table 1 in Section 3.1 of this paper. It is evident from the experimental and modeling data that both of the mechanisms are important for the degradation of phenol at the studied operating conditions. The model shows the predominance of water-splitting mechanisms for active-species (OH^*) generation at the lowest NaCl concentrations of 0.512 g L^{-1} . Under these conditions, due to the low NaCl concentration, the generation of OCl^* species is much slower. Due to species recombination, this leads to the surface being predominantly covered by OH^* , leading to OH^* -mediated reactions. As the NaCl concentrations are increased, the generation rate of the OCl^* starts to exceed that of the OH^* . This leads to a higher concentration of OCl^* on the surface and the degradation of phenol via the chlorine-species-mediated pathways. Additionally, the OCl^* recombination rates are lower than those for OH^* , as well as the phenol being more readily attacked by the OCl^* species (reaction 9 being faster than reaction 5) both lead to a predominance of the OCl^* -mediated pathways at higher NaCl concentrations. Overall, at high NaCl concentrations, the OH^* pathways are negligible, while they contribute greatly to the phenol degradation at low NaCl

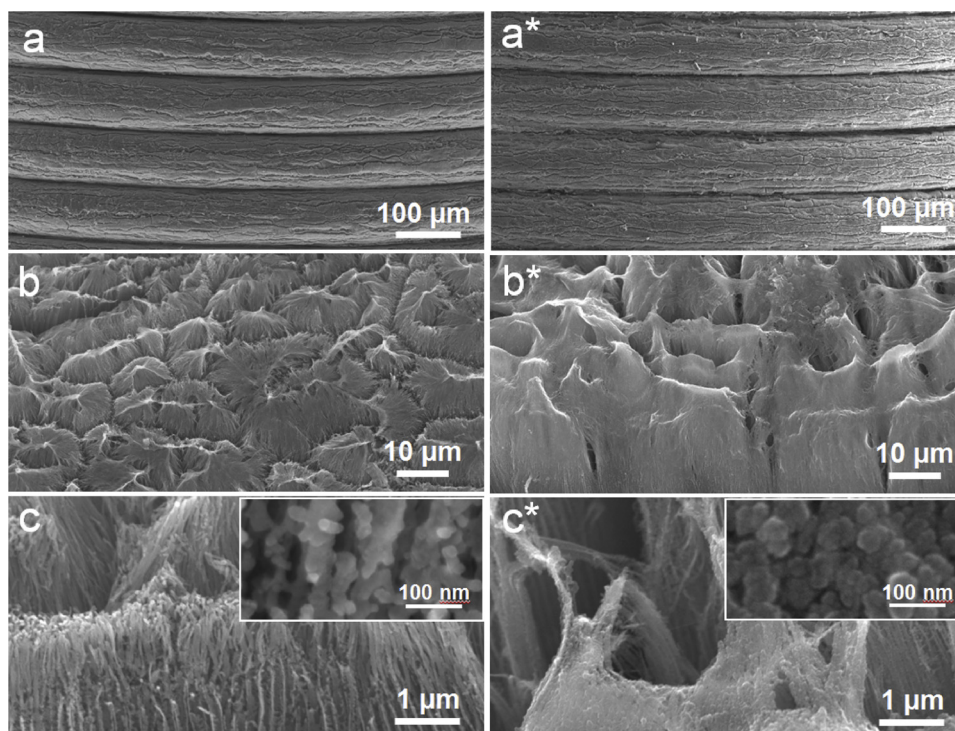


Fig. 2. FSEM micrographs of the unused and used Ti–O–N nanotube surfaces taken at different magnifications. (a,b,c) denote unused surface while (a*,b*,c*) denote used surface after the phenol-degradation tests.

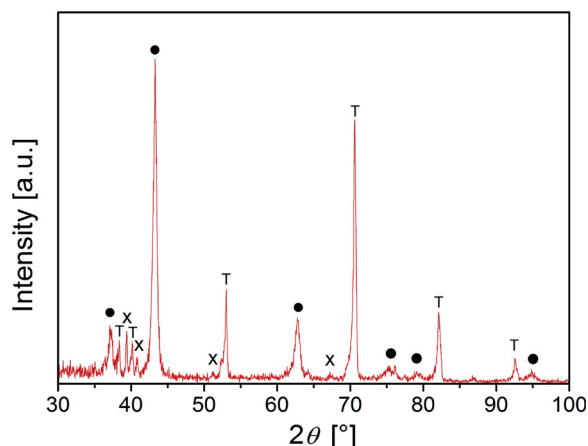


Fig. 3. XRD spectra of titanium oxynitride electrocatalyst. Peaks (circ) correspond to titanium oxynitride, peaks (T) to titanium and peaks (x) to titanium nitride.

concentrations. In the literature [35,4], it is generally observed that the chlorine-mediated mechanism is dominant at moderate Cl⁻ concentrations. Regarding the benzoquinone (BQ) concentrations, it can be observed from Table 1 that while the overall kinetics of the total oxidation through the BQ intermediate have different constant rates in the cases of OH^{*} and OCl^{*} activation, their ratios between BQ generation and consumption are similar. Therefore, similar BQ concentration profiles (Fig. S1) are observed, compared with the phenol conversion, regardless of the dominant mechanisms. However, while still negligible, it means that the role of BQ as an intermediate is higher when the OH^{*} mechanism is dominant.

Fig. 7 shows the model and experimental results for phenol degradation at different NaCl concentrations, applied voltages and flow rates. The values of the flow rates were 20, 50, 100, 200 and 500 μL min⁻¹. These flow rates correspond to the residence times of 8.3, 3.32,

1.66, 0.83 and 0.332 min, respectively. Overall, a good agreement between the model's predictions and the experimental results was obtained. There is some discrepancy between the model and experimental values at low voltages (1 V and 2 V) when high NaCl concentrations are present. This is due a combination of experimental error which is more apparent at low conversions, and the model using a linear dependence of reaction rates on voltage in order to avoid over parametrization. In the case of the experiments performed at 1 V or lower in our voltage varying experiment (Fig. 8), there was no degradation of phenol and our model assumes no reactivity. The results confirm the finding that the chlorine oxidative species play a very important role in phenol degradation. With the increasing concentration of NaCl, the phenol degradation rate is increasing. A similar situation applies to increasing the applied electrical potential, which has approximately the same effect at all NaCl concentrations. It can be seen that the model successfully captures the diminishing effect of high applied voltages at higher NaCl concentrations due to the active species' recombination and due to the degradation of more phenol, which was approaching complete decomposition. However, in any case, the increase in the applied voltage leads to a lower efficiency of the degradation process due to the competing reaction of water oxidation. During water oxidation reaction, hydrogen gas is formed at the cathode and oxygen gas at the anode. These gas is also produced when NaCl is present in the water. The reason for the formation of oxygen and not chlorine gas is that a dilute NaCl solution was used. Therefore, OH⁻ ions were selectively discharged at the anode since they are less stable than Cl⁻. The free chlorine concentration in a solution begins to increase when the NaCl concentration is 5%. In our study, the highest NaCl concentration used was 0.512%, in which case only a few ppm of free chlorine is formed [50]. The oxygen gas starts to form at the applied potential of approximately 2.1 V which is the oxygen evolution overpotential measured on the titanium oxynitride electrode [51].

The model predicts the highest phenol conversion of 97% at the most extreme operating conditions of 16 V, a NaCl concentration of 5.12 g L⁻¹, and a flow rate of 20 μL min⁻¹. Experimental result achieved at these conditions is the conversion of approximately 91.4%

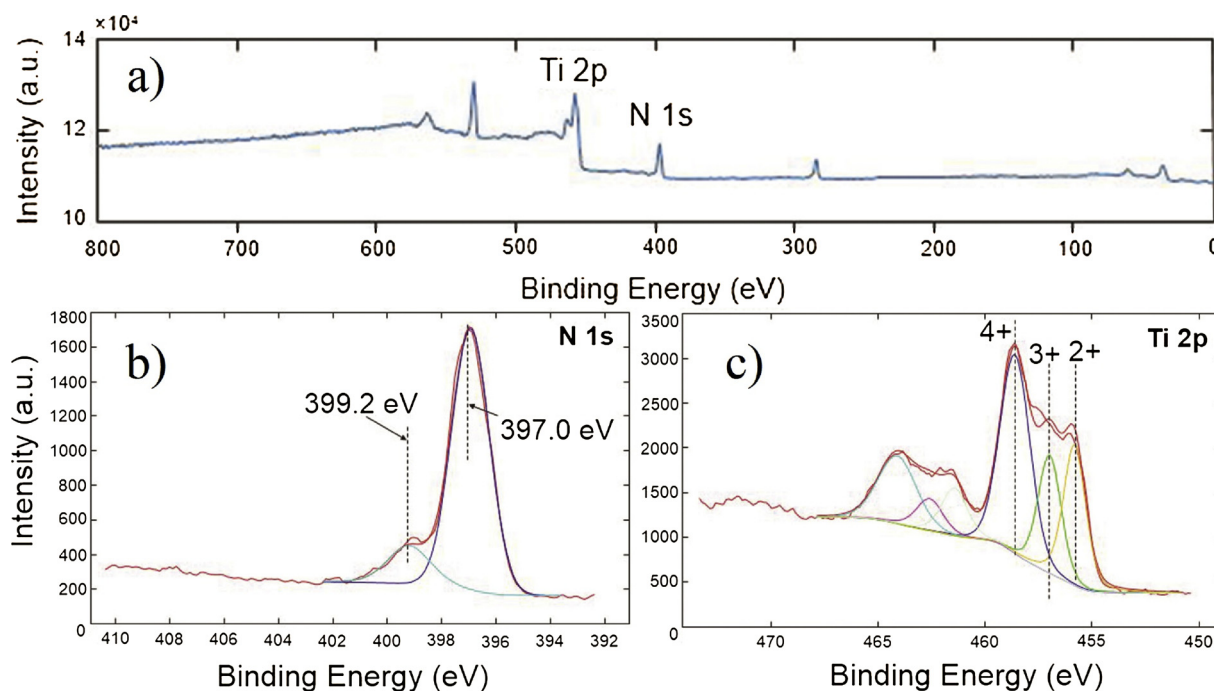


Fig. 4. XPS spectra of titanium oxynitride electrocatalyst (a), N 1s spectrum (b) and Ti 2p spectrum (c).

of the initial phenol. The experimental conversion value corresponds to the phenol removal rate of $4.81 \text{ mg L}^{-1} \text{ min}^{-1}$, whereas model predicts the phenol removal rate of $5.11 \text{ mg L}^{-1} \text{ min}^{-1}$. The removal rates are much higher than the ones determined for a coupled electro-oxidation/ozonation process, where the phenol removal rate was determined to be $0.83 \text{ mg L}^{-1} \text{ min}^{-1}$ [52]. The active component inside the electrochemical cell used for the coupled process was boron doped diamond (BDD). The authors found out that the coupled process was more efficient than electro-Fenton-like process, photo-Fenton process and heterogeneous photocatalytic process [52]. A little higher phenol removal rate (app. $1.11 \text{ mg L}^{-1} \text{ min}^{-1}$ at pH 3) was achieved with electrocatalytic process using a modified $\beta\text{-PbO}_2$ electrode [29]. The reactions were carried out under batch conditions which were also used in the study by Makgae et al. [25]. They used immobilized mixed metal oxides and achieved a rapid electrocatalytic degradation of phenol in the first two hours of experiments. Afterwards the phenol concentration reached a plateau. A complete degradation of phenol was achieved with electro-Fenton process using carbon felt cathode [24]. The authors also measured total organic carbon (TOC) which was completely removed. We

observed that the TOC value perfectly follows the results obtained by analyzing our samples with HPLC. The TOC was measured for samples obtained at the flow rate of $100 \mu\text{L min}^{-1}$, a NaCl concentration of 5.12 g L^{-1} , and various applied potentials. The HPLC results for the samples obtained at 2 V, 4 V, 8 V and 16 V show 3.7%, 23.2%, 40.3%, and 44.1% degradation of phenol, whereas the corresponding removals of TOC are 0%, 30.6%, 41.3%, and 47.2%. The amount of the formed benzoquinone was negligible, for example 0.07 mg L^{-1} was formed at applied potential of 8 V (initial phenol concentration was approximately 43.7 mg L^{-1}). Differences in the values measured with both methods occurred due to an experimental error. These results confirm the correctness of our proposed mechanism for phenol electrocatalytic oxidation on the Ti–O–N surface. The only stable by-product of phenol mineralization in this study is benzoquinone.

For shorter residence times, the high NaCl concentrations are crucial to achieve high conversions, due to the reaction rate being too slow otherwise. If the reactor is to be operated for much longer residence times, lower NaCl concentrations would be required for meaningful conversions.

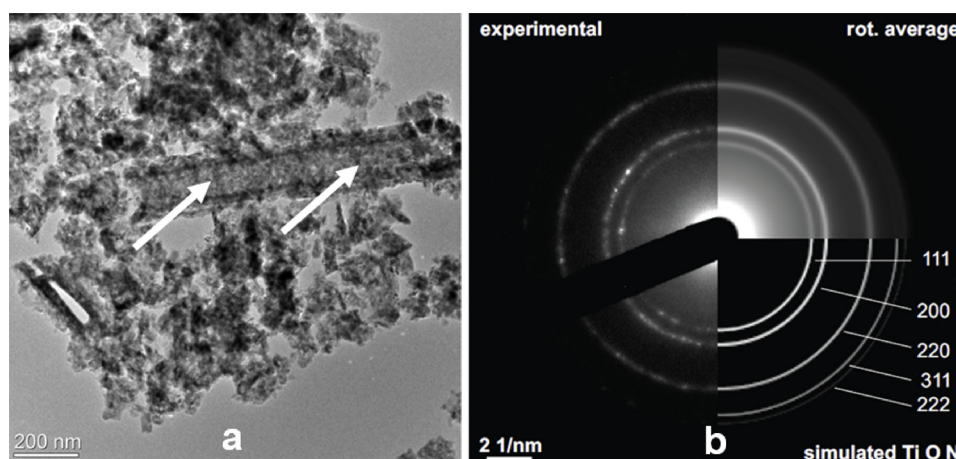


Fig. 5. (a) Bright-field TEM micrograph of Ti-O-N sample on a lacy carbon TEM grid showing nanosized Ti-O-N particles and part of the Ti-O-N nanotube marked with arrows. (b) The corresponding SAED pattern from the region in (a) confirming that the nanotubes are fully converted to oxynitride.

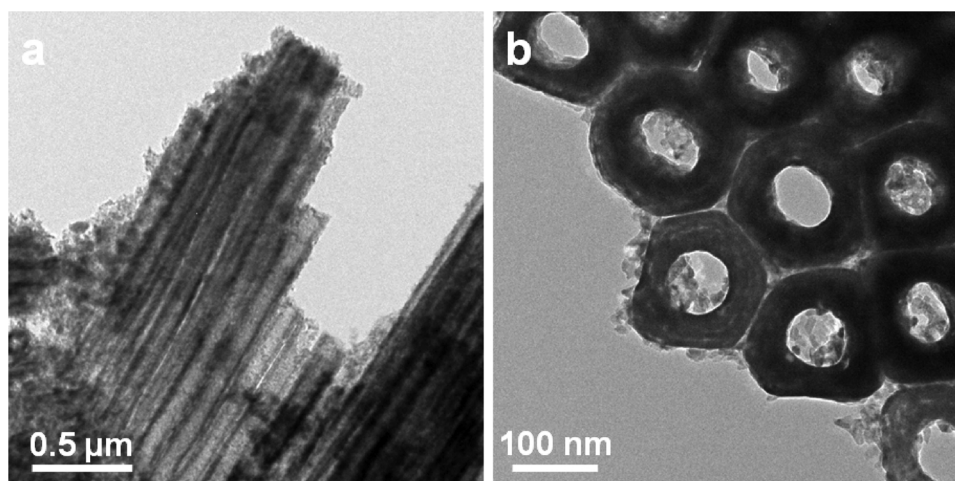


Fig. 6. (a) Bright-field TEM micrograph of Ti-O-N nanotubes. (b) Cross-section view of the Ti-O-N nanotubes.

Since the coil-type microreactor used in our study is an undivided reactor, all the reactions were taking place at the anode and cathodes in the same compartment. For this reason and due to the flow-through type of our reactor, it follows that there were no major changes in the treated solution pH during the degradation process. However, it is known that the localized pH at the anode surface is acidic, while it is

basic at the cathodes. The reduction of the pH around the anode surface is caused by the H^+ ions and the increase around the cathodes by the formation of NaOH [53]. The degradation of phenol takes place only at the anode surface [31], where the formation of OH^* species competes with the oxygen production due to water electrolysis. OCl^* species formed from Cl^- at the anode surface also significantly help degrade

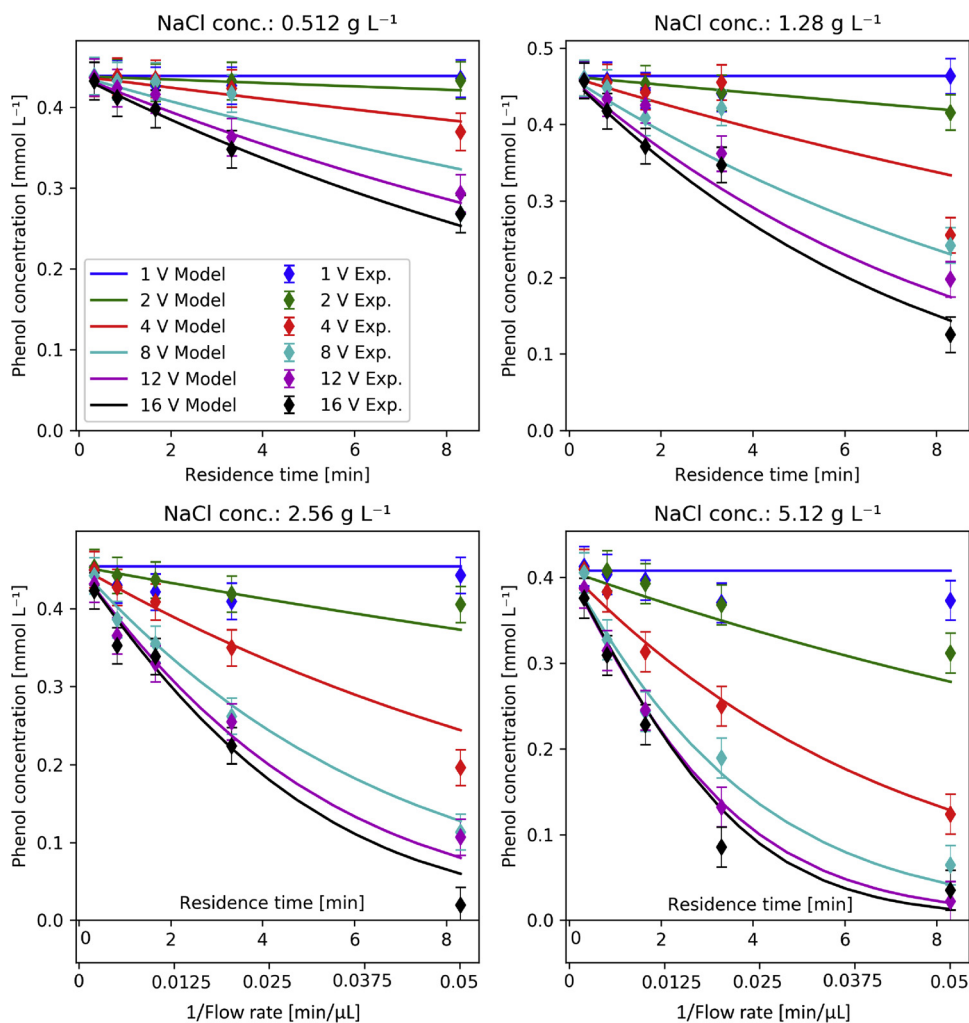


Fig. 7. Comparison between model and experimental dependence of the phenol concentration on the residence time (flow rate) at various NaCl concentrations (0.512 g/L – 5.12 g/L), applied voltages (1 V – 16 V) and liquid flow rates (20 μ L/min – 500 μ L/min).

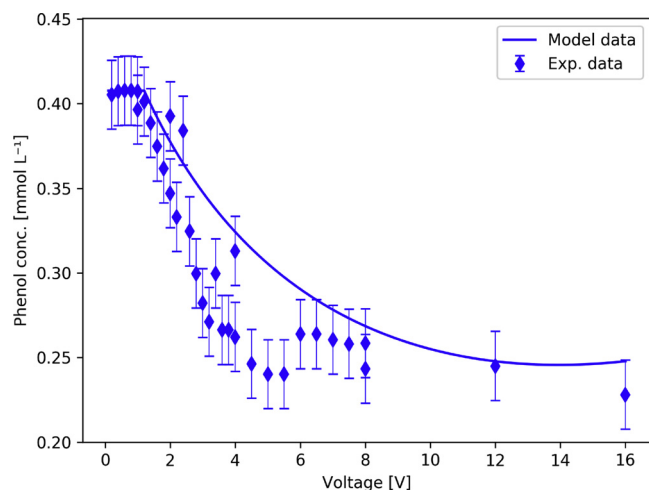


Fig. 8. Measured voltage effect on phenol degradation at $100 \mu\text{L min}^{-1}$ flow rate, 5.12 g L^{-1} NaCl concentration and varied voltage from 0.2 to 16 V.

the phenol. At the cathode, water electrolysis (hydrogen production) takes place when the applied potential is high enough. There is also the possibility for the formation of many other radicals and active species (e.g., $\text{O}_2^{\cdot-}$, OOH^{\cdot}). As mentioned above, since these species are not the dominant oxygen transfer species, the surface ones are coupled under the OH^{\cdot} and OCl^{\cdot} surface reactions and the bulk species are omitted in the model due to the surface reactions pathways being dominant. It could be argued that under some conditions or different electrode materials, the radical desorption, diffusion and bulk reaction processes would contribute greatly to the phenol degradation. In that case, our model would not be sufficiently complex to predict this behavior, and would have to be expanded with the aforementioned reactions. Some authors also report that hypochlorite can be produced electrochemically when a titanium anode and cathode are used [54]. However, we observed no degradation of the phenol when both electrodes in the coil-type microreactor were made of titanium. Also, the often-reported electrode fouling [55] during the electrocatalytic oxidation of phenol was not observed in our studies, since there was no decrease in the electrode activity. The formation of surface-fouling products was therefore not taken into account in the kinetic model.

In order to accurately determine the lowest voltage at which the phenol-degradation reaction occurs, a specific voltage-varying experiment was performed at a $100 \mu\text{L min}^{-1}$ flow rate and 5.12 g L^{-1} NaCl concentration (Fig. 8). It can be seen that there exists a cut-off voltage for a null reaction rate, which we determined was at 1.2 V using our extensive experimental data set. In addition, the voltage effect seems to stop increasing the conversion at some point. It can be observed that the model (line) correctly predicts the drop-off voltage and the general trend of the voltage effect. The voltage effect seemed to reach the plateau at lower voltages in the voltage experiment (markers); however, when all the experiments are observed in Fig. 8, there is a slight disagreement, and the model parameters were fitted to predict the behavior in all cases. Overall, the proposed OH^{\cdot} recombination mechanism can explain the behavior of the system at varying voltage fairly well.

The comparison between all the model and experimental results can be seen in Fig. 9. A parity plot and Figs. 7 and 8 show that there is good agreement between the model and the experimental results – the differences could be the consequence of either experimental error or model reaction network inaccuracy. The experimental and model concentrations of benzoquinone are presented in the supporting information (Figs. S1 and S2). It is clear that the general trends and amplitudes are captured approximately by the model, but the overall fit is relatively bad compared to the phenol case. This is due to the benzoquinone concentrations being very low, leading to a large experimental error.

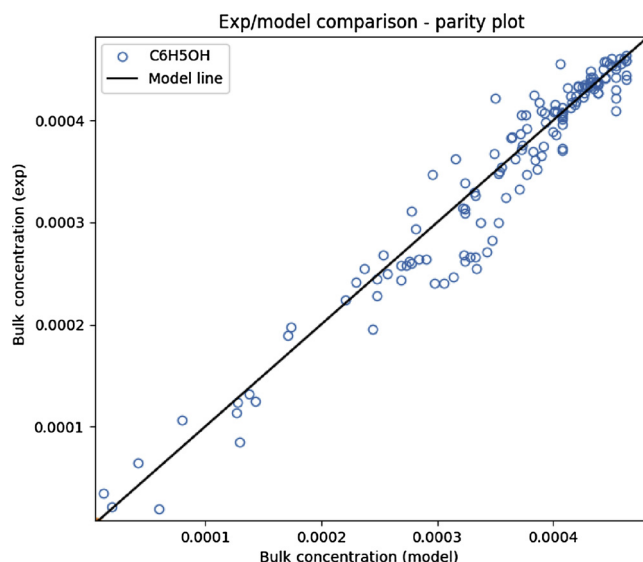


Fig. 9. Parity plot comparison between the model predictions (line) and the experimental data (markers) for phenol (including the voltage experiment data).

Additional experiments were performed in order to compare the electrocatalytic activity of Ti–O–N with that of TiO_2 nanotubes. The experiments with TiO_2 anode coil were done at the highest NaCl concentration and the flow rate of $200 \mu\text{L min}^{-1}$. The results show that electrically conductive Ti–O–N nanotubes show better activity than TiO_2 up to applied potentials of 8 V (Fig. S3). At much higher applied potential, TiO_2 nanotubes may outperform Ti–O–N due to the increased contribution to phenol degradation via the chlorine-species-mediated pathways.

4.3. Reactor design and mass-transfer limitations

It is clear from Fig. 10 that the reactor used in our experiments (gap of 0.2 mm) is still very similar in performance to an ideal plug-flow reactor with an ideal radial mass transfer. We can observe, however, that the performance starts to decrease as we further increase the gap. Due to the larger distances, the phenol cannot diffuse fast enough to the active electrode, leaving a significant portion of the phenol unreacted. This is already apparent at a distance of 0.5 mm. The exact effect of the gap distance on the reactor outlet (total) phenol conversion is presented in the bottom-right graph. The conversion is fairly constant for reactors with a gap of up to $200 \mu\text{m}$, and then it starts to rapidly decrease as larger gaps are used.

From these results it is evident that our chosen reactor gap is optimal or close-to-optimal for the phenol-degradation reaction, as using bigger gaps would induce a high mass-transfer limitation due to the radial diffusion. Therefore, for scaling up the process, numbering-up (using multiple reactors in parallel) would be the preferred strategy.

5. Conclusions

In summary, we synthesized a novel TiON electrocatalyst, performed a detailed characterization of its morphology, composition and structure, and studied its activity for the electrochemical degradation of phenol. The TiON catalyst in the form of rigidly attached, high-surface-area nanotubes was synthesized with an anodic oxidation process followed by two annealing procedures. The material possesses high electrical conductivity and is relatively easy to synthesize. This makes it a promising material that could be prepared on titanium substrates of varying shapes and sizes, to be used in reactors with different geometries for wastewater remediation. Phenol was effectively oxidized at the

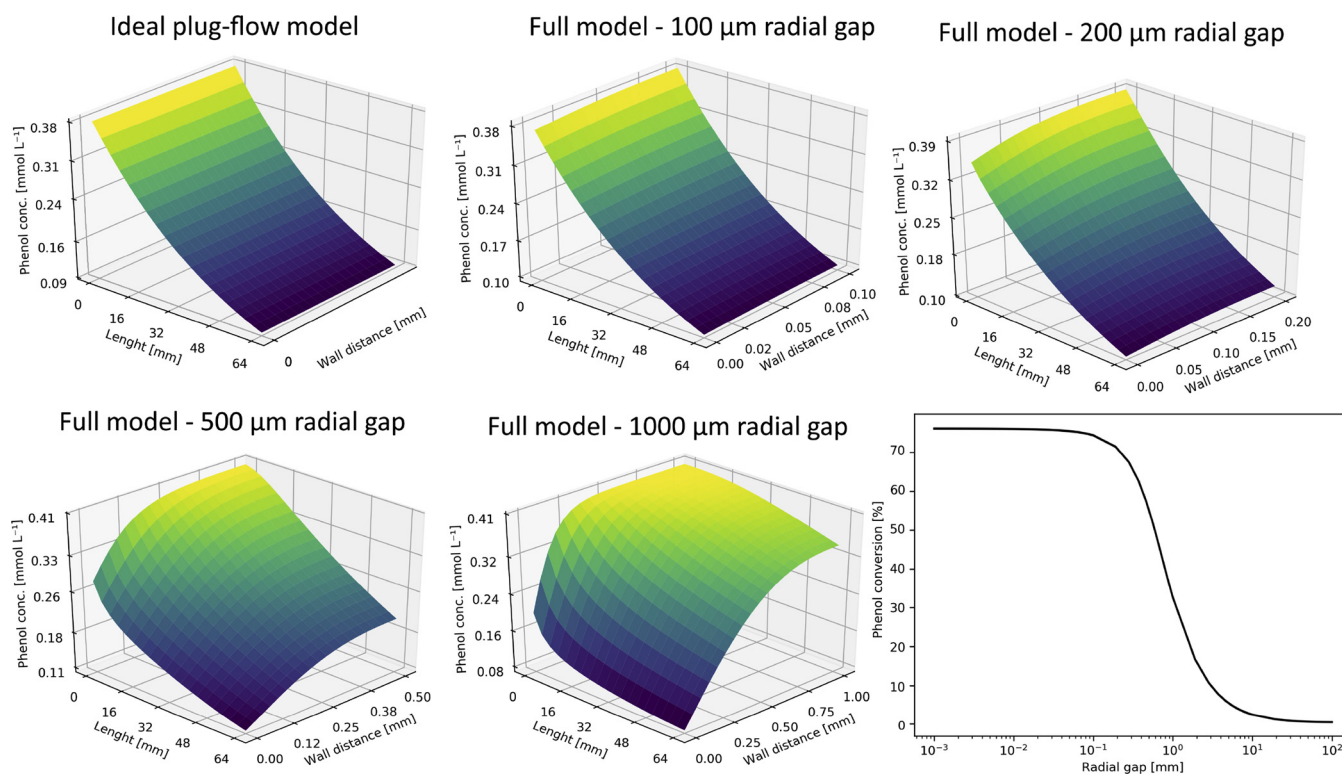


Fig. 10. Comparison of steady-state phenol concentration profiles (surface plots) and conversions (bottom-right plot) at different reactor-gap distances (distances between the inner and outer walls of the reactor). Conditions: 5.12 g L^{-1} NaCl, 16 V, 0.05 mL min^{-1} flow rate.

surface of the TiON anode with the electrocatalytically generated OH^* and OCl^* . The latter species were formed due to the presence of NaCl in the phenol solution. They significantly helped in the degradation process, which was faster with an increasing NaCl concentration. With an increasing NaCl content, the required applied voltage to achieve the same reaction rates was also lower. The only intermediate product we observed was benzoquinone. A three-dimensional kinetic-reactor model was also developed for the system, exhibiting good agreement with the experimental results. It was determined using the model that both the OH^* and OCl^* pathways contribute significantly to the phenol degradation, while the OCl^* pathways become dominant at high NaCl concentrations (5 g L^{-1}). It was also shown using the model that in terms of reactor design, the distance between the surface of the TiON coil and the inner diameter of the channel of our coil-type microreactor was close-to-optimal for the phenol-degradation reaction, as the mass-transfer limitations become significant at larger gaps. Further research will be devoted to the optimization of the synthetic conditions, with which we will determine the most appropriate ratio between titanium, oxygen and nitrogen in the Ti–O–N catalyst. Such a catalyst will then be suitable for the destruction of contaminants emerging from materials like pharmaceuticals. However, in order to commercialize the Ti–O–N catalyst, further research is needed to help reduce the cost of material production and improve its effectiveness for the degradation of organic pollutants. It is also crucial to take into account the potential risk of chlorine generation. The solution to the latter is to purify the water with a very low concentration of Cl[−] or the purification of chlorine-free wastewater.

Declaration of interests

None.

Acknowledgments

This work was supported by the Slovenian Research Agency (ARRS)

[grant numbers P2-0084, P2-0152]. The assistance of assistant professor J. Kovač is gratefully acknowledged. The authors also thank Edi Kranjc (Department of Inorganic Chemistry and Technology, National Institute of Chemistry, Slovenia) for X-ray powder-diffraction measurement.

Appendix A. Supplementary data

Supplementary material related to this article can be found, in the online version, at doi:<https://doi.org/10.1016/j.apcatb.2019.117894>.

References

- [1] Y. Yang, H. Zhang, S. Lee, D. Kim, W. Hwang, Z.L. Wang, Hybrid energy cell for degradation of methyl orange by self-powered electrocatalytic oxidation, *Nano Lett.* 13 (2013) 803–808, <https://doi.org/10.1021/nl3046188>.
- [2] R. Berenguer, J.M. Sieben, C. Quijada, E. Morallón, Electrocatalytic degradation of phenol on Pt- and Ru-doped Ti/SnO₂-Sb anodes in an alkaline medium, *Appl. Catal. B Environ.* 199 (2016) 394–404, <https://doi.org/10.1016/j.apcatb.2016.06.038>.
- [3] E. Ni, L. Qiu, Electrocatalytic oxidation of phenol in the presence of NaCl, 2010 4th Int. Conf. Bioinforma. Biomed. Eng. (2010) 1–4, <https://doi.org/10.1109/ICBBE.2010.5517061>.
- [4] M. Panizza, G. Cerisola, Direct and mediated anodic oxidation of organic pollutants, *Chem. Rev.* 109 (2009) 6541–6569, <https://doi.org/10.1021/cr9001319>.
- [5] C. Zhang, J. Wang, T. Murakami, A. Fujishima, D. Fu, Z. Gu, Influence of cations during Orange-II degradation on boron-doped diamond electrode, *J. Electroanal. Chem.* 638 (2010) 91–99, <https://doi.org/10.1016/j.jelechem.2009.10.014>.
- [6] J. Iniesta, P.A. Michaud, M. Panizza, G. Cerisola, A. Aldaz, C. Comninellis, Electrochemical oxidation of phenol at boron-doped diamond electrode, *Electrochim. Acta* 46 (2001) 3573–3578, [https://doi.org/10.1016/S0013-4686\(01\)00630-2](https://doi.org/10.1016/S0013-4686(01)00630-2).
- [7] C.-H. Lee, E.-S. Lee, Y.-K. Lim, K.-H. Park, H.-D. Park, D.-S. Lim, Enhanced electrochemical oxidation of phenol by boron-doped diamond nanowire electrode, *RSC Adv.* 7 (2017) 6229–6235, <https://doi.org/10.1039/C6RA26287B>.
- [8] X. Li, Y. Cui, Y. Feng, Z. Xie, J.-D. Gu, Reaction pathways and mechanisms of the electrochemical degradation of phenol on different electrodes, *Water Res.* 39 (2005) 1972–1981, <https://doi.org/10.1016/j.watres.2005.02.021>.
- [9] C. Comninellis, A. Nerini, Anodic oxidation of phenol in the presence of NaCl for wastewater treatment, *J. Appl. Electrochem.* 25 (1995) 23–28, <https://doi.org/10.1007/BF00251260>.
- [10] C. Comninellis, Electrocatalysis in the electrochemical conversion/combustion of

- organic pollutants for waste water treatment, *Electrochim. Acta* 39 (1994) 1857–1862, [https://doi.org/10.1016/0013-4686\(94\)85175-1](https://doi.org/10.1016/0013-4686(94)85175-1).
- [11] C. Borrás, T. Laredo, J. Mostany, B.R. Scharifker, Study of the oxidation of solutions of p-chlorophenol and p-nitrophenol on Bi-doped PbO₂ electrodes by UV–vis and FTIR in situ spectroscopy, *Electrochim. Acta* 49 (2004) 641–648, <https://doi.org/10.1016/j.electacta.2003.09.019>.
 - [12] S.Y. Yang, Y.S. Choo, S. Kim, S.K. Lim, J. Lee, H. Park, Boosting the electrocatalytic activities of SnO₂ electrodes for remediation of aqueous pollutants by doping with various metals, *Appl. Catal. B: Environ.* 111–112 (2012) 317–325, <https://doi.org/10.1016/j.apcatb.2011.10.014>.
 - [13] C. Cameselle, M. Pazos, M.A. Sanromán, Selection of an electrolyte to enhance the electrochemical decolourisation of indigo. Optimisation and scale-up, *Chemosphere* 60 (2005) 1080–1086, <https://doi.org/10.1016/j.chemosphere.2005.01.018>.
 - [14] L. Fan, Y. Zhou, W. Yang, G. Chen, F. Yang, Electrochemical degradation of aqueous solution of Amaranth azo dye on ACF under potentiostatic model, *Dyes Pigm.* 76 (2008) 440–446, <https://doi.org/10.1016/j.dyepig.2006.09.013>.
 - [15] Y. Tian, X. Chen, C. Shang, G. Chen, Active and stable Ti/Si/BDD anodes for electro-oxidation, *J. Electrochem. Soc.* 153 (2006) J80, <https://doi.org/10.1149/1.2202148>.
 - [16] F. Vaz, P. Cerqueira, L. Rebouta, S.M.C. Nascimento, E. Alves, P. Goudeau, J.P. Rivière, Preparation of magnetron sputtered TiN_xO_y thin films, *Surf. Coat. Technol.* 174 (2003) 197–203.
 - [17] M. Kot, K. Henkel, C. Das, S. Brizzi, I. Kärkkäinen, J. Schneidewind, F. Naumann, H. Gargouri, D. Schmeißer, Analysis of titanium species in titanium oxynitride films prepared by plasma enhanced atomic layer deposition, *Surf. Coat. Technol.* 324 (2017) 586–593, <https://doi.org/10.1016/j.surfcoat.2016.11.094>.
 - [18] K.A. Soliman, A.F. Zedan, A. Khalifa, H.A. El-Sayed, A.S. Aljaber, S.Y. AlQaradawi, N.K. Allam, Silver nanoparticles-decorated titanium oxynitride nanotube arrays for enhanced solar fuel generation, *Sci. Rep.* 7 (2017) 1913, <https://doi.org/10.1038/s41598-017-02124-1>.
 - [19] M. Chisaka, Y. Ando, Y. Yamamoto, N. Itagaki, A carbon-support-free titanium oxynitride catalyst for proton exchange membrane fuel cell cathodes, *Electrochim. Acta* 214 (2016) 165–172, <https://doi.org/10.1016/j.electacta.2016.08.032>.
 - [20] K.-F. Chiu, S.-H. Su, H.-J. Leu, C.-H. Hsia, Titanium oxynitride thin films as high-capacity and high-rate anode materials for lithium-ion batteries, *Thin Solid Films* 596 (2015) 29–33, <https://doi.org/10.1016/j.tsf.2015.09.083>.
 - [21] E. Martínez-Ferrero, Y. Sakatani, C. Boissière, D. Grosso, A. Fuentès, J. Fraxedas, C. Sanchez, Nanostructured titanium oxynitride porous thin films as efficient visible-active photocatalysts, *Adv. Funct. Mater.* 17 (2007) 3348–3354, <https://doi.org/10.1002/adfm.200700396>.
 - [22] C. Nunes, V. Teixeira, M.L. Prates, N.P. Barradas, A.D. Sequeira, Graded selective coatings based on chromium and titanium oxynitride, *Thin Solid Films* 442 (2003) 173–178, [https://doi.org/10.1016/S0040-6090\(03\)00967-2](https://doi.org/10.1016/S0040-6090(03)00967-2).
 - [23] Y. Saito, M. Hirata, H. Tada, M. Hyodo, Electrically switchable window using a suspension of TiO_xN_y particles, *Appl. Phys. Lett.* 63 (1993) 1319–1321, <https://doi.org/10.1063/1.109717>.
 - [24] M. Pimentel, N. Oturan, M. Dezotti, M.A. Oturan, Phenol degradation by advanced electrochemical oxidation process electro-Fenton using a carbon felt cathode, *Appl. Catal. B: Environ.* 83 (2008) 140–149, <https://doi.org/10.1016/J.APACATB.2008.02.011>.
 - [25] M.E. Makgae, M.J. Klink, A.M. Crouch, Performance of sol–gel titanium mixed metal oxide electrodes for electro-catalytic oxidation of phenol, *Appl. Catal. B: Environ.* 84 (2008) 659–666, <https://doi.org/10.1016/J.APACATB.2008.05.021>.
 - [26] C. Comninellis, C. Pulgarin, Electrochemical oxidation of phenol for wastewater treatment using SnO₂ anodes, *J. Appl. Electrochem.* 23 (1993) 108–112, <https://doi.org/10.1007/BF00246946>.
 - [27] H. Wang, Q. Guan, J. Li, T. Wang, Phenolic wastewater treatment by an electro-catalytic membrane reactor, *Catal. Today* 236 (2014) 121–126, <https://doi.org/10.1016/j.cattod.2014.05.003>.
 - [28] J. Mieluch, A. Sadkowski, J. Wild, P. Zoltowski, Electrochemical oxidation of phenol compounds in aqueous-solutions, *Przem. Chem.* 54 (1975) 513–516.
 - [29] Z. Wu, M. Zhou, Partial degradation of phenol by advanced electrochemical oxidation process, *Environ. Sci. Technol.* 35 (2001) 2698–2703, <https://doi.org/10.1021/es001652q>.
 - [30] Kabekkodu, PDF-4+, (2016).
 - [31] L. Suhadolnik, A. Pohar, B. Likozar, M. Čeh, Mechanism and kinetics of phenol photocatalytic, electrocatalytic and photoelectrocatalytic degradation in a TiO₂-nanotube fixed-bed microreactor, *Chem. Eng. J.* 303 (2016), <https://doi.org/10.1016/j.cej.2016.06.027>.
 - [32] M. Krivec, A. Pohar, B. Likozar, G. Dražić, Hydrodynamics, mass transfer, and photocatalytic phenol selective oxidation reaction kinetics in a fixed TiO₂ micro-reactor, *AIChE J.* 61 (2015) 572–581, <https://doi.org/10.1002/aic.14648>.
 - [33] X.H. Chadderdon, D.J. Chadderdon, J.E. Matthiesen, Y. Qiu, J.M. Carraher, J.-P. Tessonnier, W. Li, Mechanisms of furfural reduction on metal electrodes: distinguishing pathways for selective hydrogenation of bioderived oxygenates, *J. Am. Chem. Soc.* 139 (2017) 14120–14128, <https://doi.org/10.1021/jacs.7b06331>.
 - [34] F. Bonfatti, S. Ferro, F. Lavezzo, M. Malacarne, G. Lodi, A. De Battisti, Electrochemical incineration of glucose as a model organic substrate. II. Role of active chlorine mediation, *J. Electrochem. Soc.* 147 (2000) 592–596.
 - [35] J. Iniesta, J. González-García, E. Expósito, V. Montiel, A. Aldaz, Influence of chloride ion on electrochemical degradation of phenol in alkaline medium using bismuth doped and pure PbO₂ anodes, *Water Res.* 35 (2001) 3291–3300, [https://doi.org/10.1016/S0043-1354\(01\)00043-4](https://doi.org/10.1016/S0043-1354(01)00043-4).
 - [36] G. Fóti, D. Gandini, C. Comninellis, A. Perret, W. Haenni, Oxidation of organics by intermediates of water discharge on IrO₂ and synthetic diamond anodes, *Electrochem. Solid-State Lett.* 2 (1999) 228, <https://doi.org/10.1149/1.1390792>.
 - [37] M. Panizza, G. Cerisola, Influence of anode material on the electrochemical oxidation of 2-naphthol: part 2. Bulk electrolysis experiments, *Electrochim. Acta* 49 (2004) 3221–3226, <https://doi.org/10.1016/J.ELECTACTA.2004.02.036>.
 - [38] S.E. Treimer, J. Feng, M.D. Scholten, D.C. Johnson, A.J. Davenport, Comparison of voltammetric responses of toluene and xylenes at iron(III)-doped, bismuth(V)-doped, and undoped β-lead dioxide film electrodes in 0.50 M H₂SO₄, *J. Electrochem. Soc.* 148 (2001) E459, <https://doi.org/10.1149/1.1413991>.
 - [39] Y. Nishiki, Anodic decomposition of toxic compounds (anodic mineralization), *Encycl. Appl. Electrochem.* Springer, New York, New York, NY, 2014, pp. 78–85, https://doi.org/10.1007/978-1-4419-6996-5_338.
 - [40] M. Panizza, G. Cerisola, Electrochemical oxidation of 2-naphthol with in situ electrogenerated active chlorine, *Electrochim. Acta* 48 (2003) 1515–1519, [https://doi.org/10.1016/S0013-4686\(03\)00028-8](https://doi.org/10.1016/S0013-4686(03)00028-8).
 - [41] F. Bonfatti, A. De Battisti, S. Ferro, G. Lodi, S. Osti, Anodic mineralization of organic substrates in chloride-containing aqueous media, *Electrochim. Acta* 46 (2000) 305–314, [https://doi.org/10.1016/S0013-4686\(00\)00586-7](https://doi.org/10.1016/S0013-4686(00)00586-7).
 - [42] W.V. Smith, The surface recombination of H atoms and OH radicals, *J. Chem. Phys.* 11 (1943) 110–125, <https://doi.org/10.1021/1.1723811>.
 - [43] J. Ireneusz, D.M. Bartels, C.D. Jonah, Hydroxyl radical self-recombination reaction and absorption spectrum in water up to 350 °C, *J. Phys. Chem. A* 111 (2007), <https://doi.org/10.1021/JP065992V>.
 - [44] P. Attri, Y.H. Kim, D.H. Park, J.H. Park, Y.J. Hong, H.S. Uhm, K.-N. Kim, A. Fridman, E.H. Choi, Generation mechanism of hydroxyl radical species and its lifetime prediction during the plasma-initiated ultraviolet (UV) photolysis, *Sci. Rep.* 5 (2015) 9332, <https://doi.org/10.1038/srep09332>.
 - [45] R. Niesner, A. Heintz, Diffusion coefficients of aromatics in aqueous solution, *J. Chem. Eng. Data* 45 (2000), <https://doi.org/10.1021/JO0000569>.
 - [46] S.D. Cohen, A.C. Hindmarsh, P.F. Dubois, CVODE, a Stiff/nonstiff ODE solver in C, *Comput. Phys.* 10 (1996) 138, <https://doi.org/10.1063/1.4822377>.
 - [47] A.C. Hindmarsh, P.N. Brown, K.E. Grant, S.L. Lee, R. Serban, D.E. Shumaker, C.S. Woodward, Sundials, *ACM Trans. Math. Softw.* 31 (2005) 363–396, <https://doi.org/10.1145/1089014.1089020>.
 - [48] M.J.D. Powell, Direct search algorithms for optimization calculations, *Acta Numer.* 7 (1998) 287, <https://doi.org/10.1017/S0962492900002841>.
 - [49] T.E. Oliphant, P. Pearu, SciPy: open source scientific tools for Python, *Comput. Sci. Eng.* 9 (2001) 10–20, <https://doi.org/10.1109/MCSE.2007.58>.
 - [50] K. Whangchai, J. Uthairutra, S. Phiyanninmat, Effects of NaCl concentration, electrolysis time, and electric potential on efficiency of electrolyzed oxidizing water on the mortality of *Penicillium digitatum* in suspension, *Acta Hort.* (2013) 193–198, <https://doi.org/10.17660/ActaHortic.2013.973.26>.
 - [51] C. Gebauer, P. Fischer, M. Wassner, T. Diemant, Z. Jusys, N. Hüsing, R.J. Behm, Performance of titanium oxynitrides in the electrocatalytic oxygen evolution reaction, *Nano Energy* 29 (2016) 136–148, <https://doi.org/10.1016/J.NANOEN.2016.05.034>.
 - [52] L. Hurtado, D. Amado-Piña, G. Roa-Morales, E. Peralta-Reyes, E. Martin del Campo, R. Natividad, Comparison of AOPs efficiencies on phenolic compounds degradation, *J. Chem.* 2016 (2016) 1–8, <https://doi.org/10.1155/2016/4108587>.
 - [53] L. Suhadolnik, A. Pohar, U. Novak, B. Likozar, A. Mihelič, M. Čeh, Continuous photocatalytic, electrocatalytic and photo-electrocatalytic degradation of a reactive textile dye for wastewater-treatment processes: batch, microreactor and scaled-up operation, *J. Ind. Eng. Chem.* 72 (2019), <https://doi.org/10.1016/j.jiec.2018.12.017>.
 - [54] C.-H. Yang, C.-C. Lee, T.-C. Wen, Hypochlorite generation on Ru–Pt binary oxide for treatment of dye wastewater, *J. Appl. Electrochem.* 30 (2000) 1043–1051, <https://doi.org/10.1023/A:1004038503410>.
 - [55] J.D. Rodgers, W. Jedral, N.J. Bunce, Electrochemical oxidation of chlorinated phenols, *Environ. Sci. Technol.* 33 (1999) 1453–1457, <https://doi.org/10.1021/es9808189>.